Electronic Supplementary Information

Aqueous Synthesis of Three-Dimensional Fluorescent Silicon-Based Nanoscale Networks Featuring Unusual Anti-Photobleaching Properties

Yiling Zhong,[a] Binbin Chu,[b] Xin Bo,[a] Yao He[b] and Chuan Zhao*[a]*

[a]School of Chemistry, University of New South Wales, Sydney, NSW, 2052, Australia
E-mail: chuan.zhao@unsw.edu.au

[b]Jiangsu Key Laboratory for Carbon-Based Functional Materials and Devices, Institute of Functional Nano & Soft Materials (FUNSOM), and Collaborative Innovation Center of Suzhou Nano Science and Technology (NANO-CIC), Soochow University, Suzhou, Jiangsu 215123, China
E-mail: yaohe@suda.edu.cn

1. Experimental Section

Materials and Devices: (3-Aminopropyl)trimethoxysilane (97%) was purchased from Sigma-Aldrich. Trisodium citrate dihydrate (≥ 99%) was purchased from Ajax Finechem Pty Ltd. Zinc nitrate hexahydrate (MW 297.47, 98%) was purchased from Chem-Supply Pty Ltd (Australia). CdSe/ZnS QDs were purchased from Wuhan Jiayuan Co., Ltd. (China). 2-methylimidazole (MW 82.11, > 97%) was purchased from Tokyo chemical industry Co. Ltd.

All chemicals were used without additional purification. All solutions were prepared using Milli-Q water (Millipore) as the solvent. The microwave system Anton Paar Monowave 300 used for synthesizing silicon nanomaterials was made by Anton Paar, United States. Exclusive vitreous vessels with a volume of 10 or 30 mL are equipped for the system to provide security during reaction demanding high temperature and pressure. The SiNPs were characterized by UV-vis absorption, photoluminescence (PL), transmission electronic microscopy (TEM), high-resolution TEM (HRTEM), Brunauer-Emmett-Teller (BET), and Fourier-transform infrared (FTIR) spectroscopy. Optical measurements were performed at room temperature under ambient air conditions. UV-vis absorption spectra were recorded with a Varian Cary 100 Bio UV/Vis spectrophotometer. PL measurements were performed using a Cary Eclipse Fluorescence Spectrophotometer (Agilent). The temperature of the samples was controlled by the Varian Cary Single Cell Peltier Accessory. The PLQY of samples was estimated using quinine sulfate in 0.1 M H_2SO_4 (literature quantum yield: 58%) as a reference standard, which was freshly prepared to reduce the measurement error.[1-6] TEM and HRTEM samples were prepared by dispersing the sample onto carbon-coated copper grids with the excess solvent evaporated. The TEM/HRTEM overview images were recorded using Philips CM200 electron microscope operated at 200 kV. The Energy-dispersive X-ray (EDX) elemental mapping was recorded by JEOL JEM-F200. The specific surface area and pore size distribution were characterized by a BET analyzer (TriStar II Plus Version 2.02, MicroActive). The FTIR spectra were detected using a Nicolet iS5 FTIR spectrometer equipped with diamond ATR. The powder X-ray diffraction (XRD) spectra were recorded on a Panalytical, Empyrean, X-ray diffractometer, operated at 40 mA and 40 kV. The nanomaterials were placed on a zero-background sample holder made of monocrystal silicon plate.

Synthesis of O-SiNPs: The O-SiNPs precursor solution was prepared by adding 100 mL of (3-Aminopropyl)trimethoxysilane to 400 mL aqueous solution dispersed with 18.6 g of

trisodium citrate dihydrate. The mixture was stirred for 10 min. And then a certain amount of HCl (3 M) was added into the mixture solution to obtain the desired pH (pH = ~ 4). The pH value was monitored by Seven Multi pH meter (Mettler Toledo). The resultant precursor solution was transferred into the exclusive vitreous vessel with a volume of 30 mL. The O-SiNPs with maximum emission at ~460 nm was prepared under 180 ^{o}C/60 min. After microwave irradiation, the O-SiNPs sample was removed when the temperature cooled to < 30 ^{o}C naturally.

Surface modification of O-SiNPs: The O-SiNPs are further modified with glyoxylic acid to change the primary amine groups in the surface of the O-SiNPs into secondary amine groups. In brief, 1.2 g glyoxylic acid monohydrate was added into 240 mL solution (pH ~2.18), which include ~220 mL O-SiNPs aqueous solution and ~20 mL acetic acid, followed by 120-min stirring at room temperature. Then, the pH value of the mixture increased to ~4.5 via the addition of 1M NaOH, followed by 60-min stirring. Next, imine groups were reduced by dropwise addition of sodium borohydride (38% (w/v)), followed by 120-min stirring, producing SiNPs whose surfaces includes secondary amine groups.[7,8,9] To exclude the influences of residual reagents such as (3-aminopropyl)trimethoxysilane molecules, glyoxylic acid, and sodium borohydride, etc., the fluorescent SiNPs samples were subject to strict post-treatment before the next experiments. In details, 2-propanaol was added dropwise under stirring until the sample solution became slightly turbid. The turbid dispersion was continually stirred further for 10 min. The precipitate fraction of the sample was isolated from the supernatant by centrifugation. This procedure was repeated three times. The purified SiNPs precipitates were re-dispersed in water.

Formation of the three-dimensional fluorescent SiNNs: The SiNNs precursor solution was prepared by 4 mL of the SiNPs (optical density value: 3.2) to 12 mL aqueous solution dispersed with 269 μmol zinc nitrate and 3.9 mmol 2-methylimidazole. The resultant precursor solution was transferred to the exclusive vitreous vessel with a volume of 30 mL.

The SiNNs were prepared under 120 ^{o}C/1 h. After microwave irradiation, the SiNNs sample was removed when the temperature cooled to less than 30 ^{o}C naturally. Subsequently, three centrifugations and washing steps with Milli-Q water were performed to remove the residual reagents, such as free SiNPs, zinc nitrate, and 2-methylimidazole. The purified SiNNs were re-dispersed in Milli-Q water.

Photostability: To guarantee reliable comparison, the PL intensity of SiNPs, FITC, CdSe/ZnS QDs and SiNNs was adjusted to the similar value. The four samples were continuously irradiated for different time intervals using UV light 365 nm.

The photostability of the solid SiNNs powder. A bamboo pattern was designed and printed on using a commercial printer. 10 mg the solid SiNNs powder was dispersed in 1mL water-ethanol mixtures (V_{water}:$V_{ethanol}$ = 4). The resultant high concentration SiNNs solution was painted on the bamboo pattern by using a paint brush. And then the bamboo pattern painted with SiNNs was dried at room temperature. The bamboo pattern coated with SiNNs powder was continuously irradiated for different time intervals using UV light 365 nm.

Optical measurements and TEM characterizations of the fluorescent SiNNs: Optical measurements were performed at room temperature under ambient air conditions. UV-vis absorption spectra were recorded with a Varian Cary 100 Bio UV/vis spectrophotometer. 600 µL solution of the prepared SiNNs sample was transferred into an exclusive Quartz cuvette for UV spectra measurements. Photoluminescence (PL) measurements were performed using a Cary Eclipse Fluorescence Spectrophotometer (Agilent). 3 mL solution of the prepared SiNNs sample was transferred into an exclusive quartz cuvette for PL spectra measurements. TEM and HRTEM samples were prepared by dispersing the sample onto-carbon-coated copper grids with the excess solvent evaporated. The TEM/HRTEM over-view images were recorded using Philips CM 200 electron microscopy operated at 200 kV.

MTT assay of cell viability: Colorimetric 3-(4,5-dimethylthiazol-2-yl)-2,5-diphenyl tetrazolium bromide (MTT, Sigma-Aldrich) assay, recognized as an established method, was

employed for assessment of cytotoxicity in our experiment. In brief, Cells (e.g., HeLa cells, MCF-7) dispersed in 96-well cell-culture plate at 1.5×10^4/well were cultured at 37 ^oC for 12 h under 5% CO_2. Thereafter, SiNNs of serial concentrations (18, 36, 78, 156, 312 μg/mL) were added into each cell and co-incubated with Cells for 3, 6, 12, 24 h in a humidified atmosphere at 37 ^oC with 5% CO_2. The assay was based on the accumulation of dark-blue formazan crystals inside living cells after exposure to MTT, which is a well-established protocol for assessment of cellular viability. Destruction of cell membranes by the addition of sodium dodecylsulfate resulted in the liberation and solubilization of crystals. The number of viable cells was thus directly proportional to the level of the initial formazan product created. The formazan concentration was finally quantified using a spectrophotometer by measuring the absorbance at 570 nm (ELISA reader). A linear relationship between cell number and optical density was established, thus allowing for accurate quantification of changes in the rate of cell proliferation. To ensure reproducibility, three independent experiments were performed, and all measurements were carried out in triplicate.

In vitro cell imaging of the SiNNs: Human cervical cells (HeLa cells) and Human breast adenocarcinoma cells (MCF-7 cells) were selected as the target cells, which were cultured in Dulbecco's modified Eagle's medium with high glucose (H-DMEM) and improved RPMI-1640 medium, respectively. These mediums were supplemented with 10% heat-inactivated fetal bovine serum (FBS), 100 μg/mL streptomycin and 100 U/mL penicillin. Finally, these all cell lines were cultured at 37 °C in an incubator containing 5% CO_2, respectively. For in vitro cell imaging in live cells, the target cell lines (e.g., HeLa and MCF-7 cells) were incubated with pure medium (control group) or 150 μg/mL SiNNs for 12 h at 37 °C. Then, the labeled cells were mounted on slides in fluoromount (Sigma, F4680) with coverslips. In vitro imaging was performed with a confocal laser microscope (Leica, TCS-SP5 II) and imaging was carried out under 30% power of argon laser. For SiNNs channel, diode laser ($\lambda_{excitation}$ = 405 nm) was used as the excitation light source and collect the fluorescence excitation of

SiNNs at 550-650 nm. To guarantee no cell fluorescence background of live HeLa cells was detected, we set the offset at -3.5%.

In vivo tumor imaging of the SiNNs: 4T1 tumor (mouse invasive breast cancer)-bearing mice were used as models in our experiment. For in vivo tumor imaging, 0.1 mL cell suspension containing 4T1 cells were subcutaneously injected into the right abdomen region of Balb/c mice (female, 4-5 weeks old). After the mice whose tumor size was up to ~500-600 mm^3, they would be intratumorally administered with physiological saline (control group) or the SiNNs (200 μL, 4 mg/mL), and imaged by a Maestro EX in vivo fluorescence imaging system (CRi, Inc.). Mice were purchased from Nanjing Peng Sheng Biological Technology Co. Ltd. and used under protocols approved by Soochow University Laboratory Animal Center.

LIVE SUBJECT STATEMENT

All experiments involving live subjects (i.e., mice) were performed in Soochow University in compliance with the relevant laws and institutional guidelines of Soochow University Laboratory Animal Center. The Soochow University Laboratory Animal Center has approved the experiments outlined in this work. No human subjects were used in this work.

2. Supplementary Figures

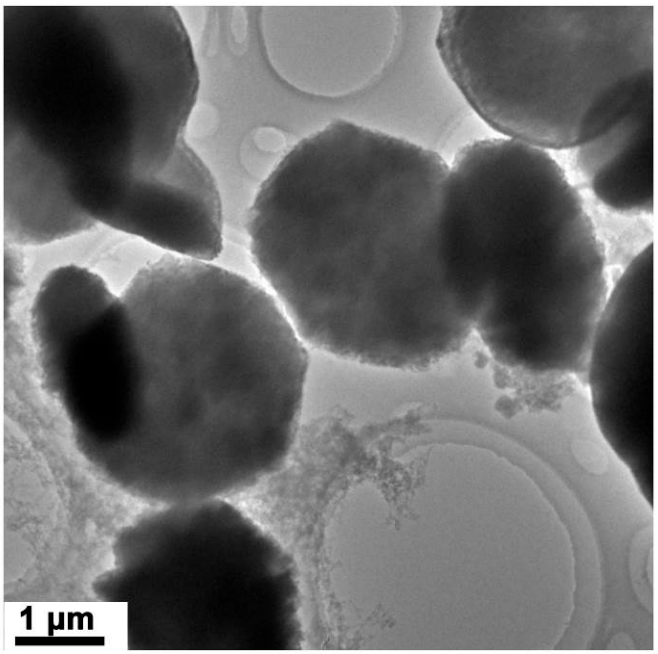

Fig. S1 TEM image of the control group. TEM micrographs of nanomaterials synthesized using the mixture of zinc nitrate, 2-methylimidazole, and the O-SiNPs. As shown in Fig. S1, random aggregations are observed, indicating that the O-SiNPs are difficultly assembled to SiNNs under the same experimental condition.

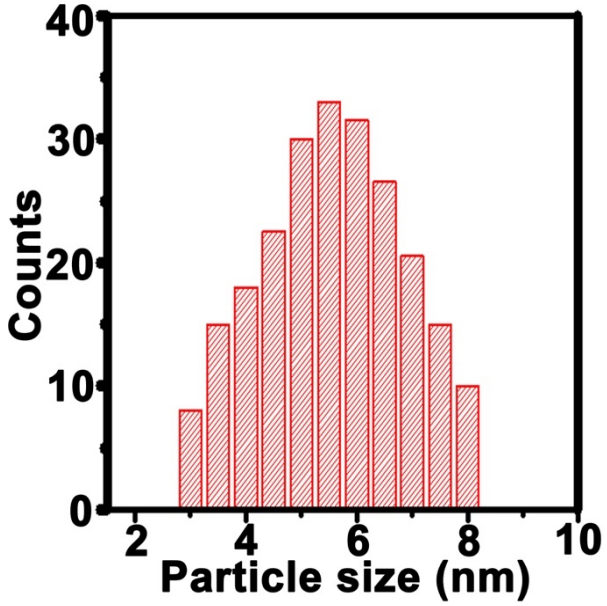

Fig. S2 The TEM diameter distribution of the fluorescent SiNPs.

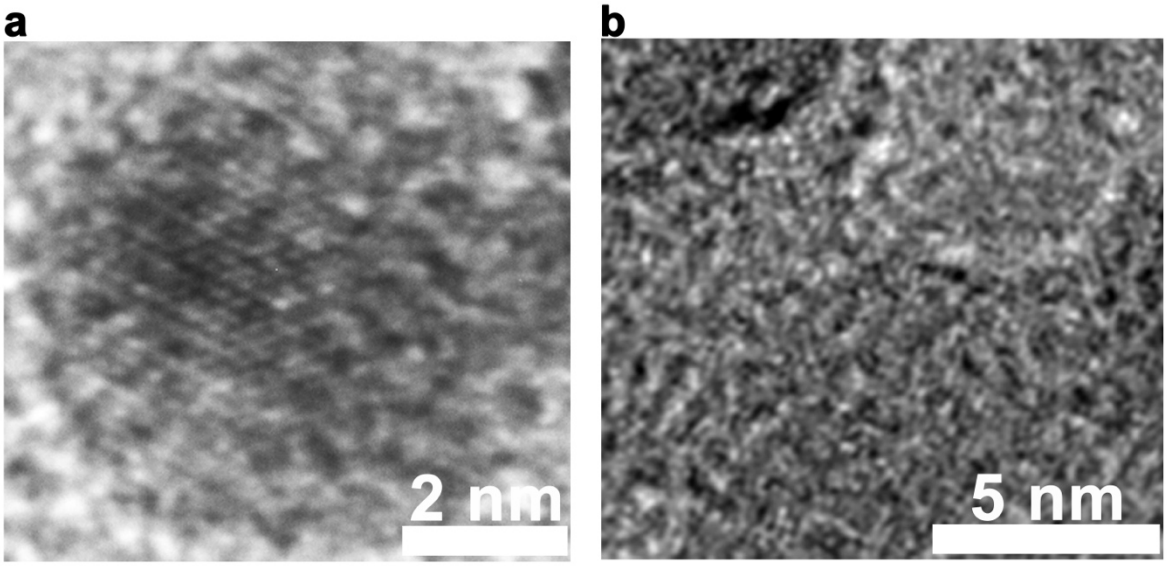

Fig. S3 The enlarged HRTEM images of the fluorescent SiNPs (a) and the as-prepared SiNNs (b).

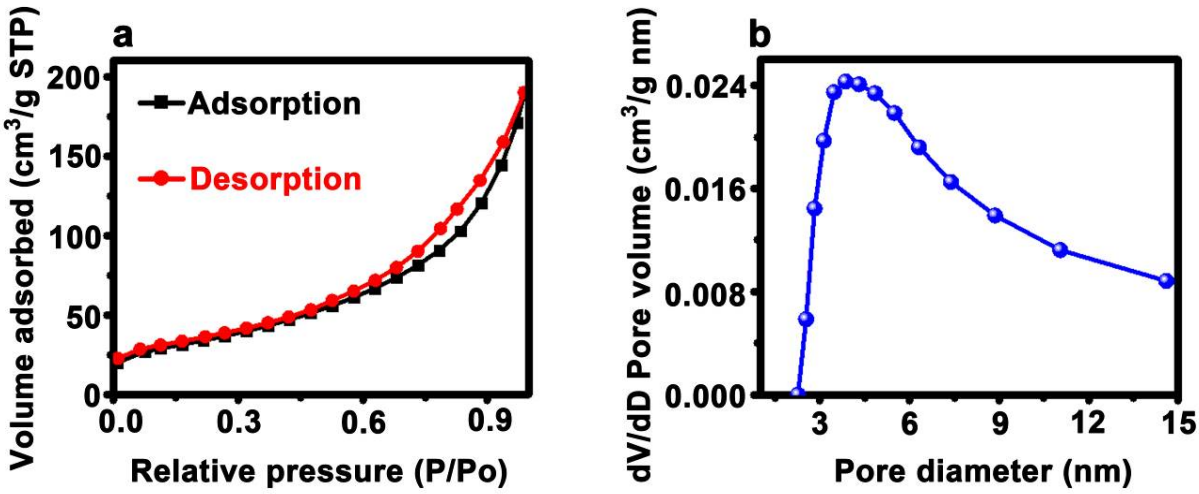

Fig. S4 BET characterization. (a) Nitrogen adsorption-desorption isotherms and (b) BJH pore size distribution calculated from N_2 adsorption isothermals of the as-prepared SiNNs.

The surface area is one of the most important quantities for characterizing novel porous materials. Surface areas are commonly reported as Brunauer-Emmett-Teller (BET) surface areas obtained by applying the theory of Brunauer, Emmett, and Teller to nitrogen adsorption isotherms measured at 77 K. In our case, nitrogen adsorption-desorption isotherms as shown in Fig. S4a are measured to evaluate the surface area and the pore size distribution of the SiNNs sample. As shown in Fig. S4a the general shape of the N_2 sorption isotherms for the SiNNs suggests the existence of different pore sizes spanning from micro to macropores. Hysteresis between adsorption and desorption branches can be observed at medium relative pressure, which demonstrates the existence of mesoporous. The almost vertical tails at the relative pressure near to 1.0 point to the presence of macroporosity. The pore size distributions of the SiNNs sample calculated from the nitrogen adsorption branch is shown in Figure S4b. The majority of pores are located in the region of mesopore. The BET surface area and the Barrett-Joyner-Halenda (BJH) average pore size of SiNNs are 120 m^2/g, and 6.3 nm, respectively.[10-13]

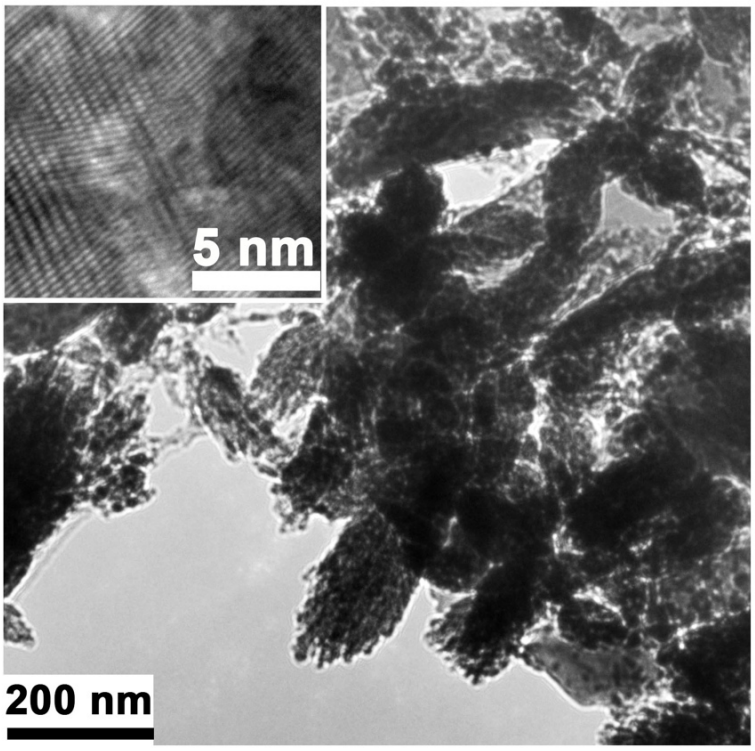

Fig. S5 TEM and HRTEM images of the control group. TEM and HRTEM images of the ZnMOFs synthesized using the mixture of zinc nitrate and 2-methylimidazole.

To understand the SiNNs formation process, we carried out a series of control experiments. As shown in Fig. S5, random aggregates (metal-organic frameworks (ZnMOFs)) instead of networks are obtained when microwave-assisted synthesis was performed with zinc nitrate and 2-methylimidazole, in the absence of fluorescent SiNPs. HRTEM image (Fig. S5, inset) shows the synthesized ZnMOFs possess well-resolved lattice fringes, and good crystallinity. Similarly, no network structures can be formed with a mixture of zinc nitrate and fluorescent SiNPs, without 2-methylimidazole molecules (Fig. S6a). Finally, network structures cannot be observed under the same experimental conditions using 2-methylimidazole and the fluorescent SiNPs as reaction precursors, due to lack of coordinated metal ions (Fig. S6b).

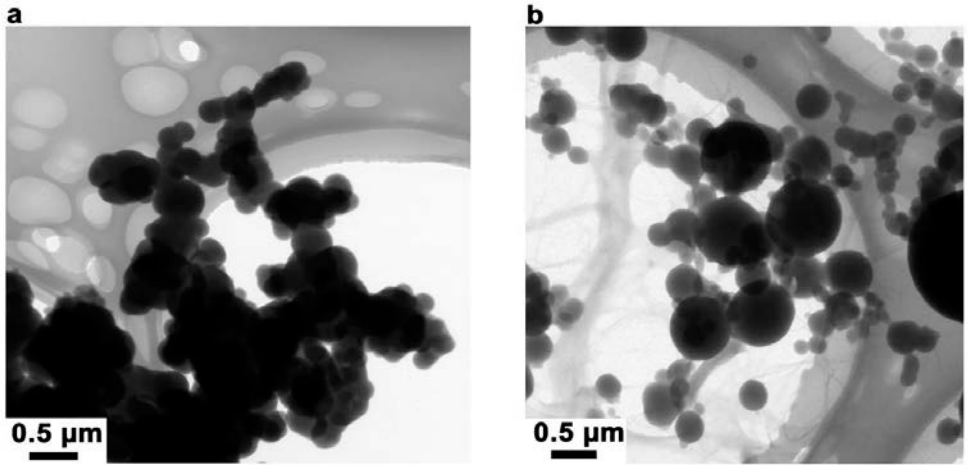

Fig. S6 TEM image of the control group. TEM micrographs of nanomaterials synthesized using (a) the mixture of the fluorescent SiNPs and zinc nitrate, (b) the fluorescent SiNPs with 2-methylimidazole.

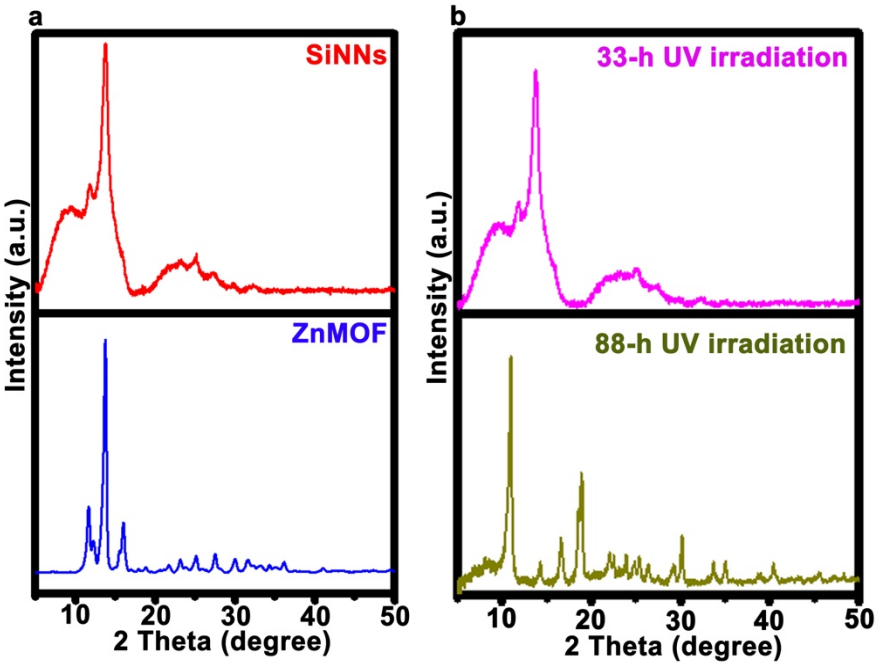

Fig. S7 (a) XRD patterns of the resultant SiNNs, and ZnMOFs synthesized using the mixture of zinc nitrate and 2-methylimidazole samples. (b) XRD patterns of the 33- and 88-h UV irradiated SiNNs.

As shown in Fig. S7a, the XRD patterns of SiNNs exhibit less characteristic and sharp diffraction peaks owing to the low crystallinity, which is consistent with the HRTEM result of SiNNs. In comparison the XRD patterns of ZnMOFs (blue line) features characteristic and sharp diffraction peaks at 11.6°, 13.8°, 16.2°, and etc, indicating the crystallinity of ZnMOFs.[14,15] Taken together with TEM/HRTEM results, these findings reveal that the SiNNs are amorphous structure with low crystallinity. Furthermore, the XRD patterns of the UV irradiated SiNNs are interrogated, as shown in Fig. S7b. The 33-h UV irradiated SiNNs (Fig. S7b, pink line) have almost the same characteristic peaks as the 0-h UV irradiated SiNNs (Fig. S7a, red line). However, the UV irradiated SiNNs exhibit characteristic and sharp diffraction peaks when the irradiation time extend to 88h (Fig. S7b), which are similar to that of ZnMOF. Taken together with the FTIR and EDX results (Fig. S8, and S11), these findings suggest that the structures of the SiNNs are damaged after 88-h UV irradiation, and zinc oxide and/or ZnMOF structures should be formed.[14,15]

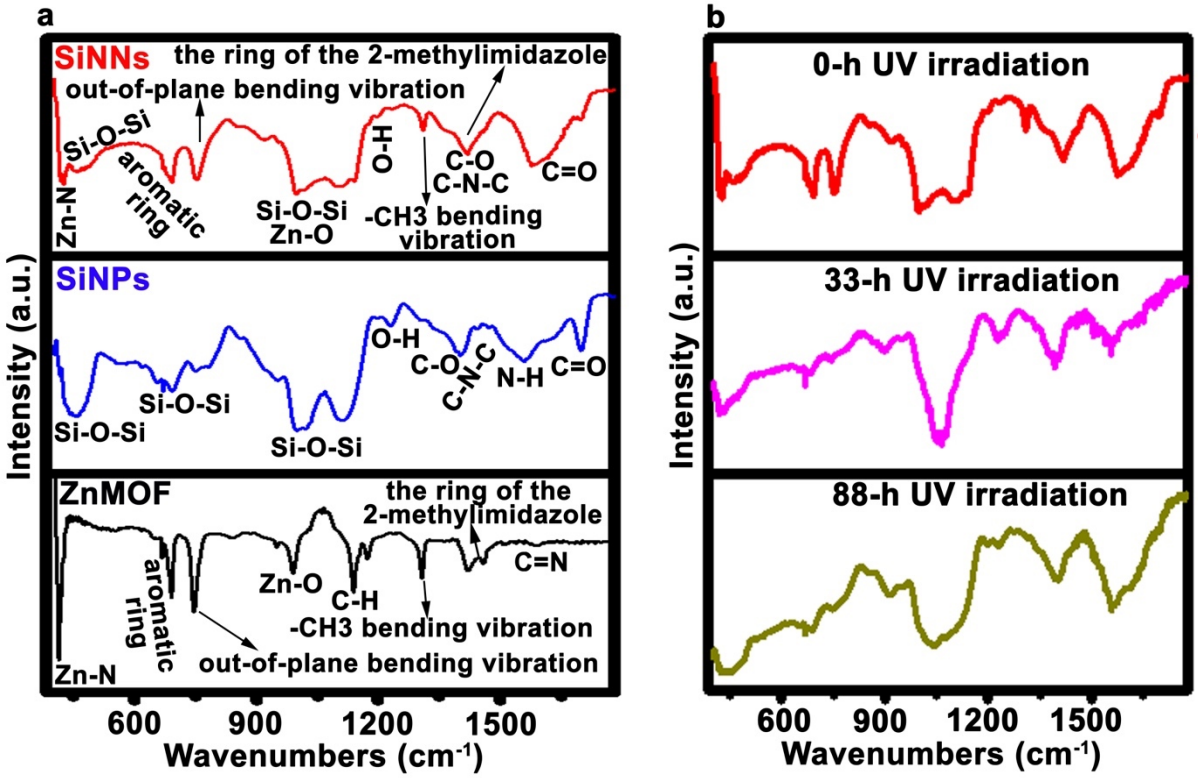

Fig. S8 (a) FTIR spectra of the SiNNs, SiNPs, and ZnMOFs synthesized using the mixture of zinc nitrate and 2-methylimidazole, exhibiting obvious absorption peaks at 400-1800 cm^{-1}. (b) FTIR spectra of the 0-h, 33-h, and 88-h UV irradiated SiNNs. Note: the FTIR spectra of the 0-h UV irradiated SiNNs (b, red line) and the SiNNs (a, red line) are same.

To interrogate the surface functional groups of SiNNs, the FTIR spectroscopy are further applied. The FTIR spectra of the SiNPs, ZnMOF, and SiNNs exhibit strong absorption peaks in the range of 400-1800 cm^{-1} (Fig. S8a). The characteristic FTIR peaks of the SiNPs (Fig. S8a, blue line) located at around 465, 800, and 1090 cm^{-1} are related to asymmetric, symmetric, and bonding modes of Si-O-Si bridging sequences, respectively. The absorbance at circa 1236, 1390, 1420, 1580, and 1690 cm^{-1}, can be assigned to the deformation vibration of O-H bonding, the bending vibration of C-O bonding, C-N-C vibration, N-H bending vibrations, and C=O stretching vibration, respectively.[1-6] For ZnMOFs (Fig. S8a, black line), the strong FTIR absorbance peaks at around 420, 690, 740, 990, 1150, 1320, 1390-1500, and

1590 cm^{-1} are assigned to the vibration of Zn-N bonding, the vibration of aromatic ring, the out-of-plane bending vibration of ZnMOF, the vibration of Zn-O bending, the in-plane vibration of ZnMOF, $-CH_3$ bending vibration, the stretching of the ring of 2-methylimidazole, and the stretching vibration of C=N bonding, respectively. The FTIR peaks of the as-prepared SiNNs (Fig. S8a, red line) can be assigned to the vibration of Zn-N bonding (421 cm^{-1}), the vibration of asymmetric of Si-O-Si bridging sequences (450-600 cm^{-1}), the vibration of aromatic ring (690 cm-1), the out-of-plane bending vibration of SiNNs (750 cm^{-1}), the vibrational stretch of Si-O-Si/the vibration of Zn-O (990-1160 cm^{-1}), the deformation vibration of O-H bonding (1180-1270 cm^{-1}), $-CH_3$ bending vibration (1310 cm^{-1}), the stretching of the ring of 2-methylimidazole/the bending vibration of C-O bonding/C-N-C vibration (1380-1500 cm^{-1}), and C=O stretching vibration (1590 cm^{-1}), respectively.[1-6,16-20] Furthermore, the FTIR spectra of the 33-h and 88-h UV irradiated SiNNs are further investigated. In comparison to the 0-h UV irradiated SiNNs (Fig. S8a and b, red line), the FTIR spectra of the UV irradiated SiNNs make changes to some extent, as shown in Fig. S8b. Typically, the two characteristic peaks between 420-600 cm^{-1} are broadened and merged into a single peak after UV irradiation. The peaks located at 690 and 750 cm^{-1}also are broadened and almost merged into a single peak. Moreover, the characteristic peaks of Zn-O (990-1160 cm^{-1}) is gradually enhanced with increasing irradiation time.

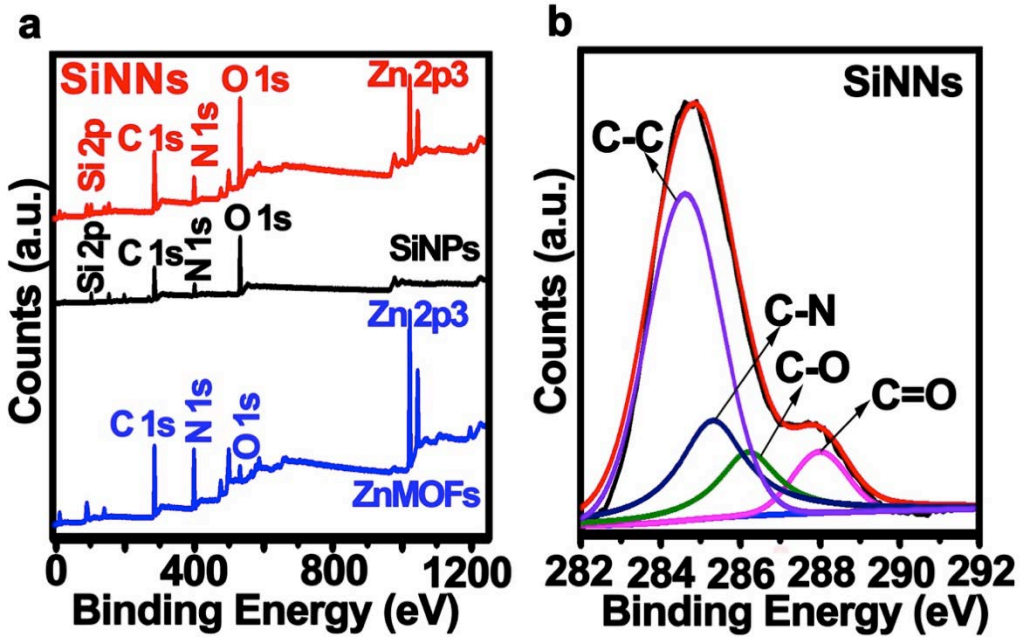

Fig. S9 XPS characterization. (a) XPS spectra of the SiNNs, SiNPs, and ZnMOF. (b) C 1s spectra of the as-prepared SiNNs.

Fig. S9 displays the XPS spectra of the SiNPs (black line), ZnMOFs (blue line), and SiNNs (red line). Specifically, Fig. S9a (black line) presents the XPS spectra of the SiNPs, exhibiting four distinct peaks located at 103 eV, 286 eV, 401 eV, and 533 eV, which are ascribed to Si 2p, C 1s, N 1s, and O 1s, respectively. The XPS spectra of ZnMOF is displayed in Fig. S9a (blue line), in which C 1s, N 1s, O 1s, and Zn 2p3 produce four peaks at 286 eV, 401 eV, 533 eV, and 1025 eV, respectively. For the resultant SiNNs, five characteristic peaks at 103 eV, 286 eV, 401 eV, 533 eV, and 1025 eV (ascribed to Si 2p, C 1s, N 1s, O 1s, and Zn 2p3, respectively) are observed (red line), demonstrating the existence of C, O, N, Si, and Zn elements in the SiNNs. Notably, Fig. S9b presents the typical C 1s spectrum of SiNNs, exhibiting four distinct peaks located at 284.6, 285.3, 286.2, and 288.6 eV, which are assigned to C-C, C-N, C-O, and C=O, respectively.[21-27]

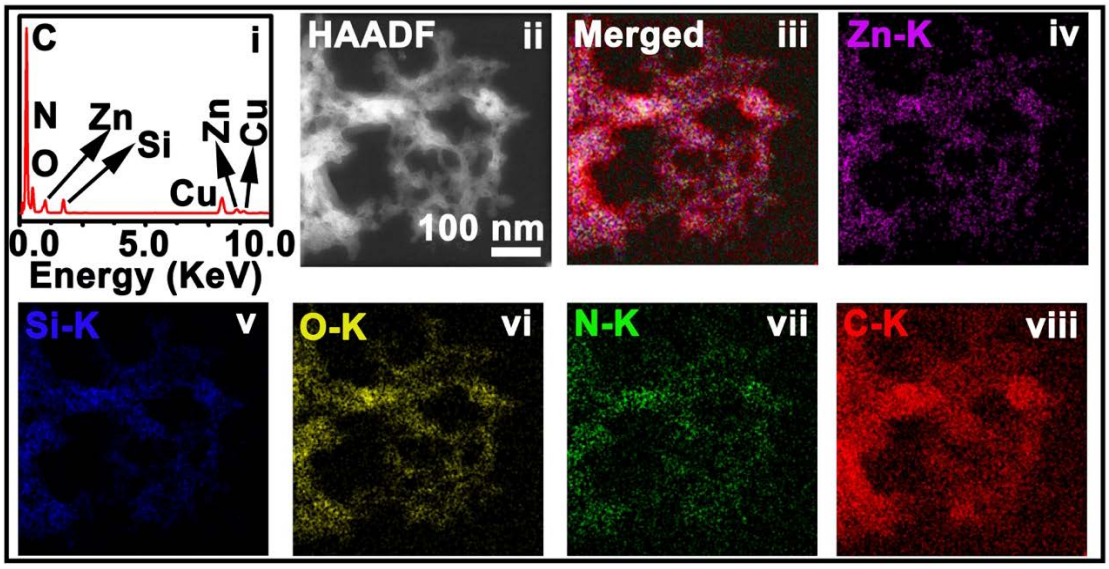

Fig. S10 High-angle annular dark-field image and corresponding EDX element mapping images, as well as EDX pattern of the resultant SiNNs. The EDX mapping analyses are further performed to determine the local composition of the as-prepared SiNNs. As shown in Fig. S10, the EDX results further qualitatively demonstrate the existence of Si, O, N, C, and Zn elements in the SiNNs. The distribution of Zn and N elements is consistent with that of Si, attributed to the interaction of the fluorescent SiNPs with metal ions.

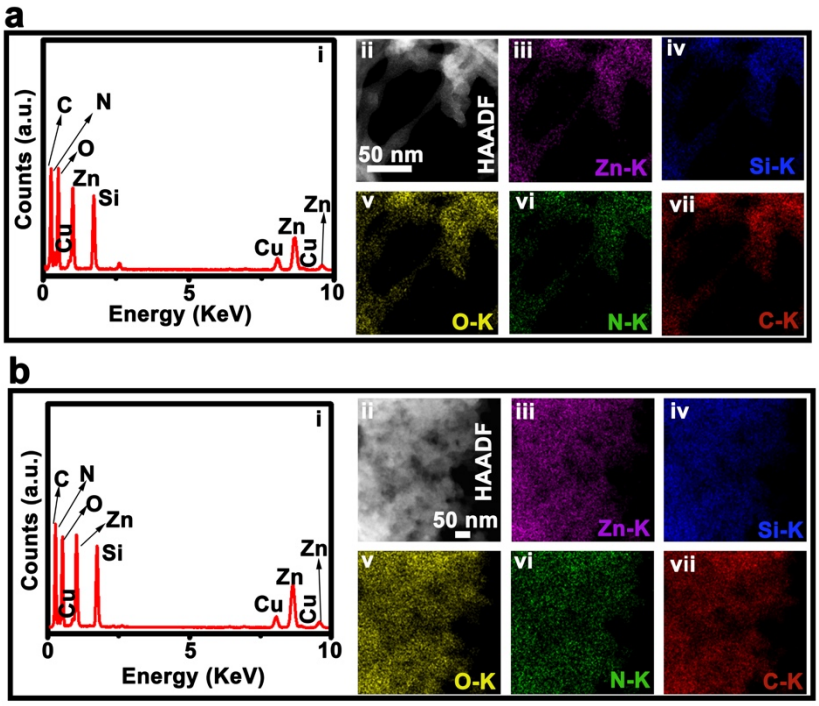

Fig. S11 High-angle annular dark-field images and corresponding EDX element mapping images, as well as EDX pattern of the 33-h (a) and 88-h (b) UV irradiated SiNNs. As shown in Fig. S11, the EDX results qualitatively indicate that the existence of Si, O, N, C, and Zn elements in the UV irradiated SiNNs. Remarkably, for EDX testing, a quantitative analysis of the elemental ratios is not possible since the supporting substrate (e.g., carbon-coated copper grid) is carbon containing a measurable amount of residual oxygen.[4]

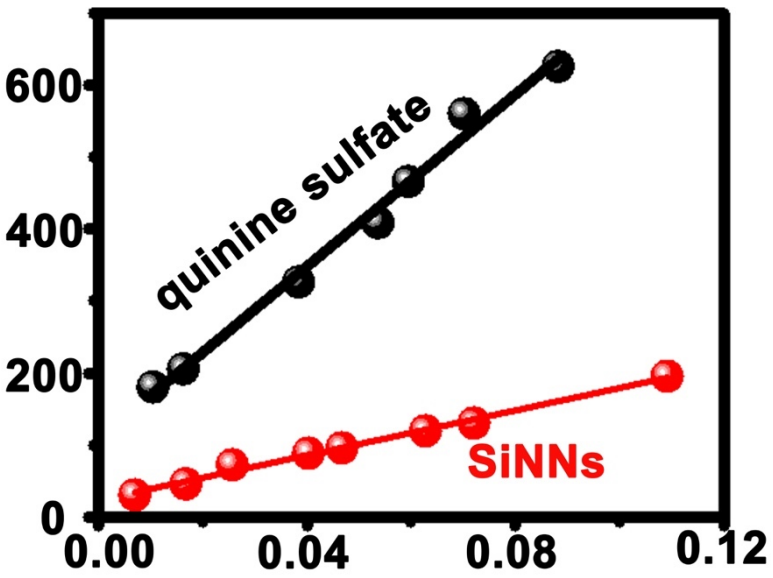

Fig. S12 PLQYs measurements of the SiNNs. A typical example of integrated PL intensity dependence on the absorbance for the SiNNs (red line), and quinine sulfate (black line) in 0.1M H_2SO_4. The solid lines represent the fitting results for each set of data. PLQYs of the SiNNs are calculated by using the equation: $Q_x=Q_r(M_x/M_r)(n_x/n_r)^2$. Where n is the average refractive index of the solvent (for these aqueous solutions, $n_x/n_r = 1$), M is the gradient of straight line, Q is quantum yield, and the subscripts x and r refer to the test samples and reference solutions, respectively.

Fig. S13 Photographs of ZnMOFs under ambient light (right) and 365 nm irradiation. The aqueous solution dispersed with the ZnMOFs is obviously turbid and exhibits weak fluorescence under UV irradiation.

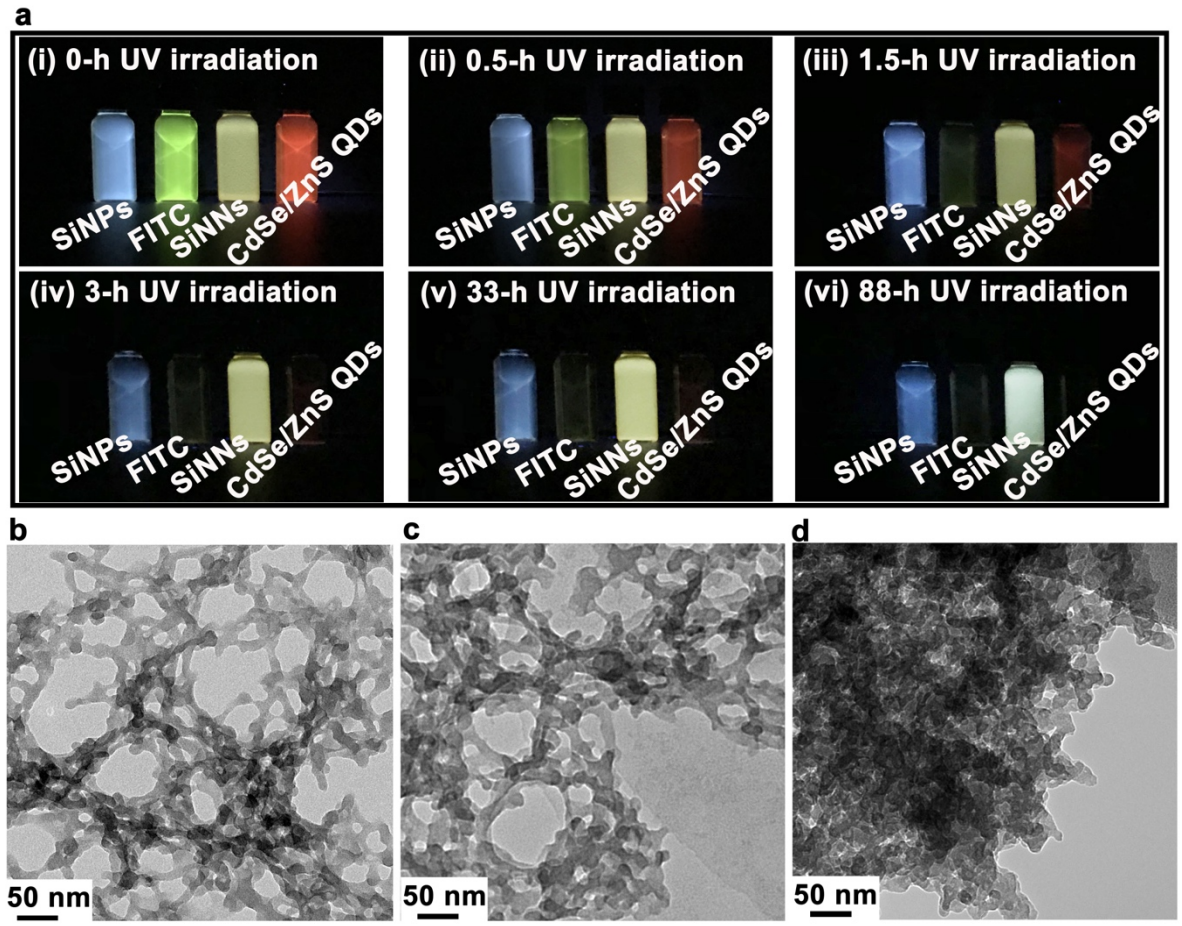

Fig. S14 (a) Photographs of SiNPs, FITC, CdSe/ZnS QDs and SiNNs samples for different UV irradiation time. (b-d) TEM images of the SiNNs for 0-h, 33-h and 88-h UV irradiation, respectively.

Fig. S14a shows the photographs of the four samples of SiNPs, FITC, CdSe/ZnS QDs, and SiNNs under UV irradiation. Notably, while all the samples show distinct fluorescence during initial UV irradiation, the fluorescent signals of the two control samples (i.e., FITC and CdSe/ZnS QDs) almost disappear after 1.5-, and 3-h UV irradiation, respectively. SiNPs control group is more stable. The fluorescent signal decreases gradually with irradiation time but still can be observed after long-term (e.g., 33 h and 88 h) UV irradiation. In remarkable contrast, the fluorescent signals of the SiNNs sample doesn't decrease at all, instead it enhances during long-time irradiation under the same experiment conditions. Specifically, the

SiNNs sample displays stronger yellow fluorescence after UV irradiation for 33 h (Fig. S14a, (v) 33-h UV irradiation). While the luminesce color changes slightly, the SiNNs exhibits stronger and brighter fluorescence after 88-h UV irradiation (Fig. S14a, (vi) 88-h UV irradiation).

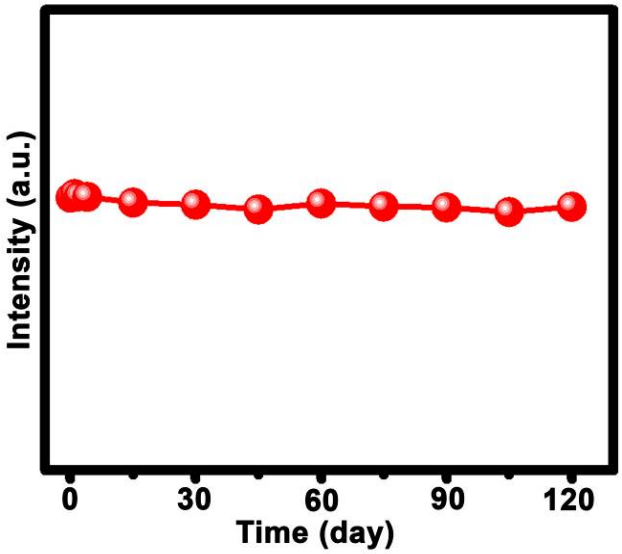

Fig. S15 Storage stability. The as-prepared SiNNs sample retains nearly identical fluorescent intensity during 120 days of storage.

We further test the storage stability of the SiNNs. Shown in Fig. S15, the as-prepared SiNNs preserve extremely stable optical properties during long-term storage. The SiNNs maintain high and stable PL intensity during the 120 days storage in the ambient environment without any protection. This excellent fluorescent storage-stability is crucial for practical applications.

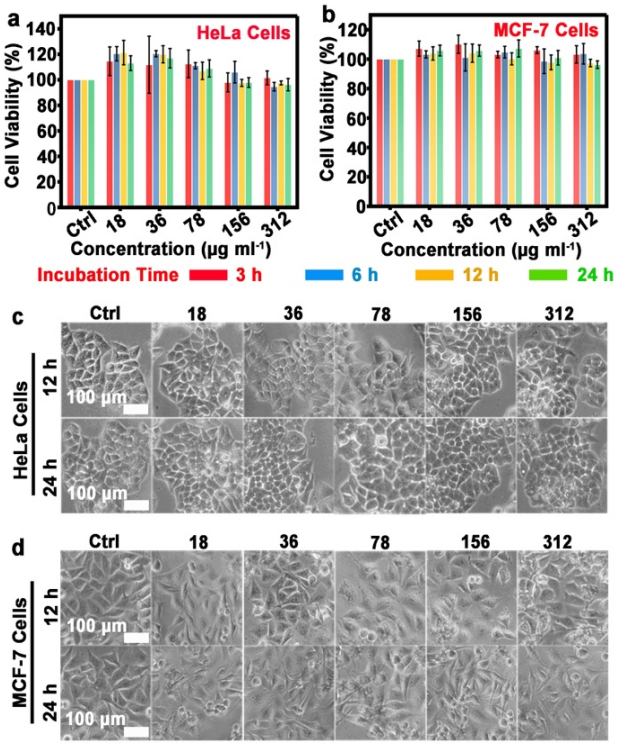

Fig. S16 Cytotoxicity assessment of the as-prepared SiNNs. Cytotoxicity of HeLa cells (a) and MCF-7 cells (b) treated with the SiNNs of serial concentrations for different incubation time, respectively. Morphology of HeLa cells (c) and MCF-7 cells (d) after incubated with SiNNs of serial concentrations for 12, 24 h, respectively.

As biocompatibility is essential to biomedical applications, we thus further evaluate the cytotoxicity of the prepared SiNNs. Specifically, we test cellular toxicity of the resultant SiNNs with different concentrations (e.g., 18, 36, 78, 156, and 312 μg/ml) using established MTT assay. Fig. S12a and b show that the cell viabilities of HeLa cells and MCF-7 cells both maintain above 95% during 24-h incubation with SiNNs, whose concentration ranges from 18 μg/ml to 312 μg/ml. Microscopic studies confirmed the biochemical assays of cellular viability. As shown in Fig. S12c and d, no obvious morphological change of HeLa cells and MCF-7 are observed in the presence of SiNNs, when the concentration of SiNNs increase to 312 μg/ml, and the incubation time is extended to 24 h. In addition, we interrogate in vitro toxicity of the UV irradiated SiNNs. Fig. S17 shows that the cell viability of HeLa cells and

MCF-7 cells both maintain above 85% during 24-h incubation with the UV irradiated SiNNs (i.e., 33- and 88-h UV irradiated SiNNs), whose concentration ranges from 18 to 312 μg/ml. Moreover, the SiNNs and UV irradiated SiNNs show low cellular toxicity to non-cancer cells (i.e., ARPE-19 cells) during 24-h incubation with nanomaterials (i.e., SiNNs (Fig. S18a), 33-h (Fig. S18b) and 88-h (Fig. S18c) UV irradiated SiNNs). Fig. S18 shows that the cell viability of non-cancer cells maintains above 85% during 24-h incubation with SiNNs and UV irradiated SiNNs. In comparison to the cancer cells (Fig. S16a and b), the non-cancer cells (Fig. S18a) exhibit slightly lower cell viability during 24-h incubation with SiNNs. The cytotoxicity of the UV irradiated SiNNs to non-cancer cells is similar to that of the UV irradiated SiNNs to cancer cells during 24-h incubation with the UV irradiated SiNNs. These data suggest low cytotoxicity of the SiNNs and the UV irradiated SiNNs to the cells (cancer cells and non-cancer cells), which can be attributed to the favorable biocompatibility of silicon and zinc.[1-6,29-32]

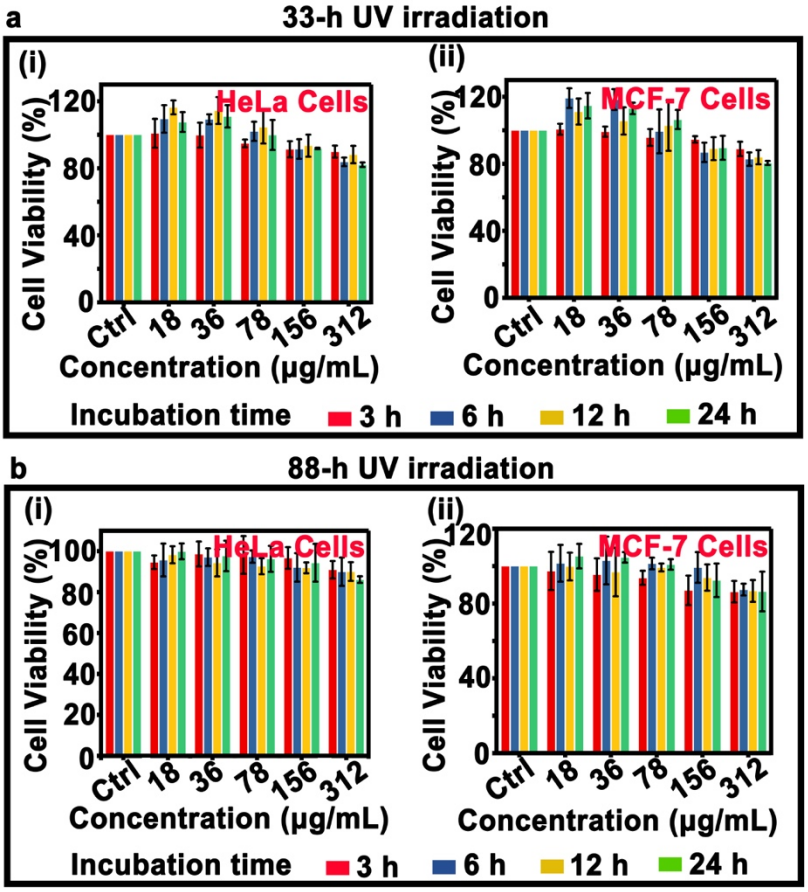

Fig. S17 Cytotoxicity assessment of the UV irradiated SiNNs. Cytotoxicity of HeLa cells (i) and MCF-7 cells (ii) treated with the 33-h (a) and 88-h (b) UV irradiated SiNNs of serial concentrations for different incubation time respectively.

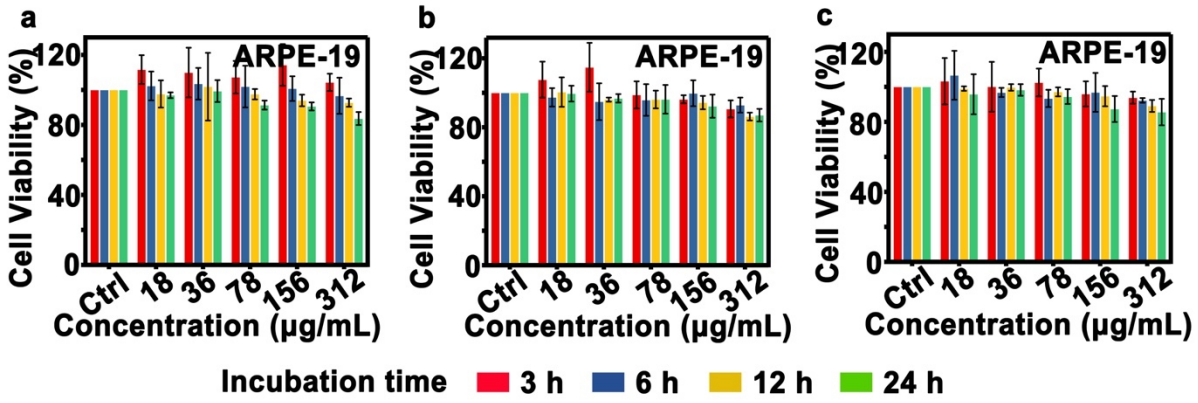

Fig. S18 Cell viability of ARPE-19 cells treated with the 0-h (a), 33-h (b) and 88-h (c) UV irradiated SiNNs of serial concentrations for different incubation time respectively.

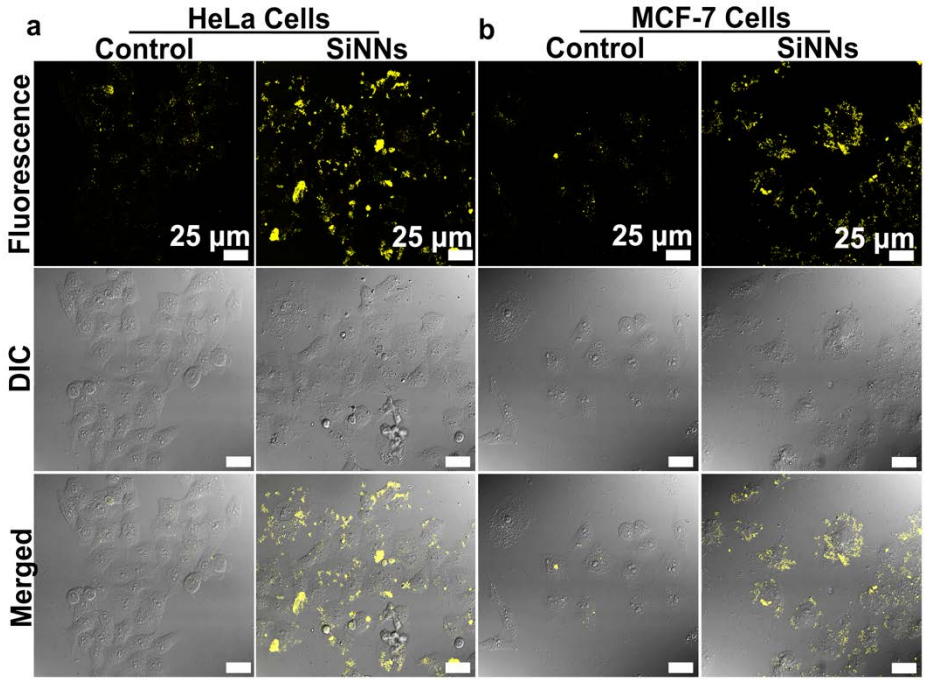

Fig. S19 Internalization of the SiNNs in live cells. (a) Fluorescence imaging of the SiNNs in live HeLa cells. HeLa cells are treated by pure medium (control group) or the SiNNs for 12 h. (b) Fluorescence imaging of the SiNNs in live MCF-7 cells. MCF-7 cells are treated by pure medium (control group) or the SiNNs for 12 h. Scale bars, 25 μm.

As shown in Fig. S19a, compared with the feeble yellow fluorescence signals of HeLa cells in the control groups, the SiNNs-treated HeLa cells show distinct yellow fluorescence signals in cytoplasm. In addition, obvious yellow fluorescence is detected in the cytoplasm of SiNNs-treated MCF-7 cells, while the control groups display no obvious yellow signals (Fig. S19b). These findings demonstrate that the resultant SiNNs are able to be uptaken by live cells and distribute in cytoplasm to some extent, suggesting that the SiNNs can be used for cell imaging.

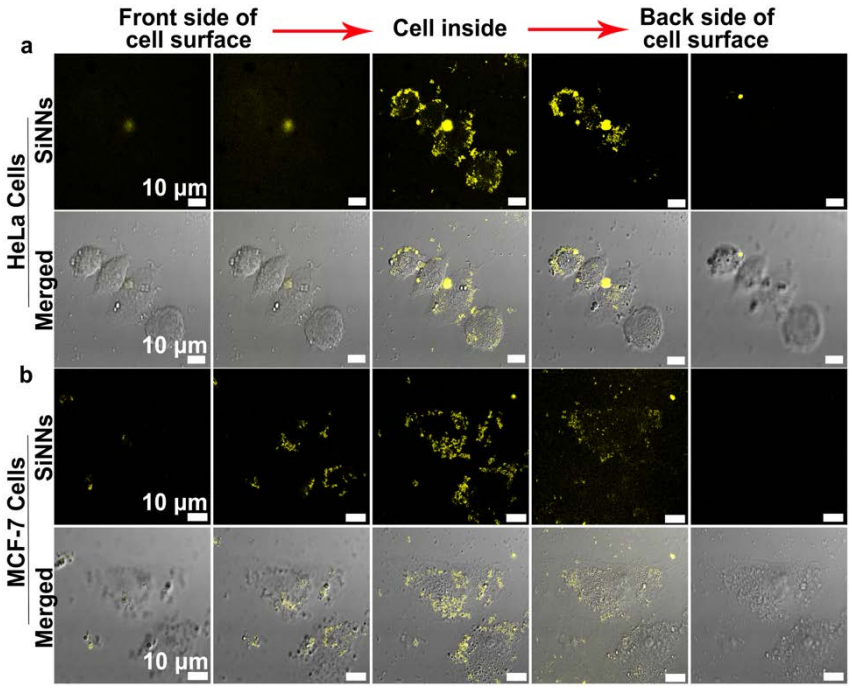

Fig. S20 Three-dimensional confocal images of live cells treated by the SiNNs. Confocal pictures of cell imaging of the SiNNs versus the changes of Z-axis in HeLa cells (a) and MCF-7 cells (b), respectively. Scale bar, 10 μm.

As presented in Fig. S20, the weak yellow signals are able to be observed on the front side of the cell surface. As the scan proceeds towards the inner layer of HeLa cells (a) and MCF-7 cells (b), the intensity of yellow luminescence gradually increases. When the Z-axis changes to the cell inside, the strongest yellow fluorescence signals can be imagined in HeLa cells (a) and MCF-7 cells (b). After that, the yellow fluorescence signals become weaker as the scan proceeds to the back side of the cell surface. These results reveal that the prepared SiNNs are able to enter into the cell and finally locate in cytoplasm, rather than simply absorbing to the cell surface.

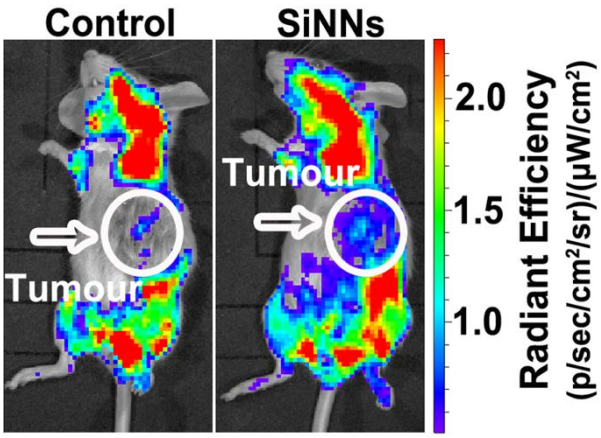

Fig. S21 In vivo tumor imaging of the SiNNs. In vivo imaging of the mouse treated by physiological saline (control group, left) and the SiNNs (right) under the same conditions. As shown in Fig. S21, no obvious fluorescence signal is observed in tumor tissues of the control group. In contrast, the SiNNs-treated mouse exhibit distinct fluorescence signals in tumor tissues, revealing that the as-prepared SiNNs can be as a promising fluorescent probe for in vivo imaging.

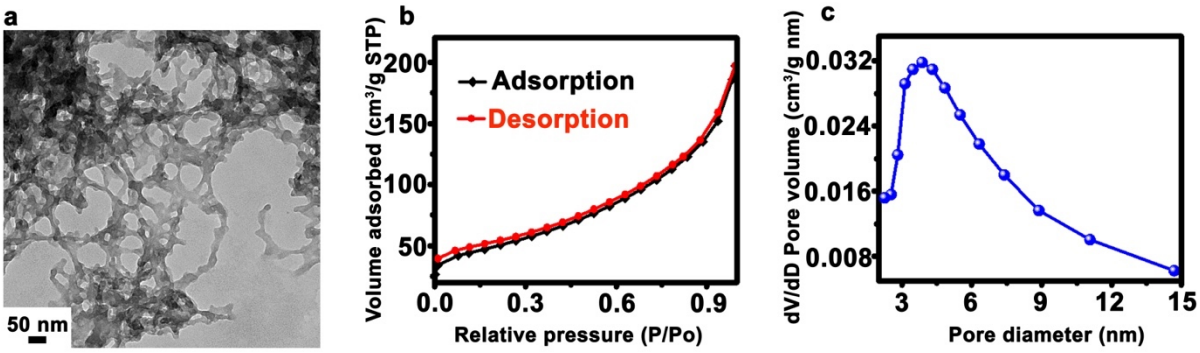

Fig. S22 (a) TEM image of the SiNNs synthesized under 120 ^{o}C/ 3 h. (b) Nitrogen adsorption-desorption isotherms and (c) BJH pore size distribution calculated from N_2 adsorption isothermals of the SiNNs synthesized under 120 ^{o}C/ 3 h.

Fig. S22a shows the TEM image of the SiNNs synthesized under 120 ^{o}C/3h, in which the SiNNs appear as network structure. As shown in Fig. S22b the general shape of the N_2 sorption isotherms for the SiNNs synthesized under 120 ^{o}C/3h suggests the existence of different pore sizes spanning from micro to macropores. The pore size distributions of the SiNNs sample (120 ^{o}C/3h) calculated from the nitrogen adsorption branch is shown in Fig. S22c. The majority of pores are located in the region of mesopore. The BET surface area and the Barrett-Joyner-Halenda (BJH) average pore size of SiNNs are 174 m^2/g, and 5.5 nm, respectively.[10-13] These experimental results indicate that the surface area and pore size of the SiNNs can be tuned through the adjustment of the reaction time.

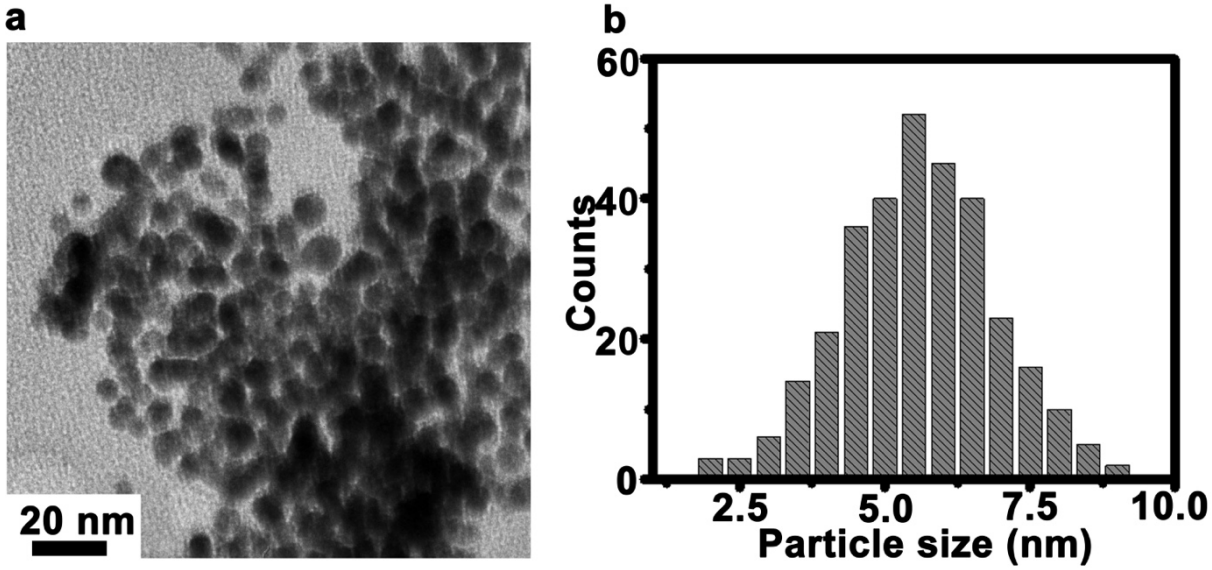

Fig. S23 TEM image (a) and size distribution (b) of the fluorescent SiNPs, which are prepared under 180 ^{o}C/ 2h. Fig. S23a shows the TEM image of the fluorescent SiNPs prepared under 180 ^{o}C/2h, in which the as-prepared SiNPs appear as spherical particles. The size distribution calculated by measuring more than 300 particles shows an average diameter of ~5.6 nm. The fluorescent SiNPs prepared under 180 ^{o}C/2h have almost the same size as the fluorescent SiNPs synthesized under 180 ^{o}C/1h (~5.5 nm).

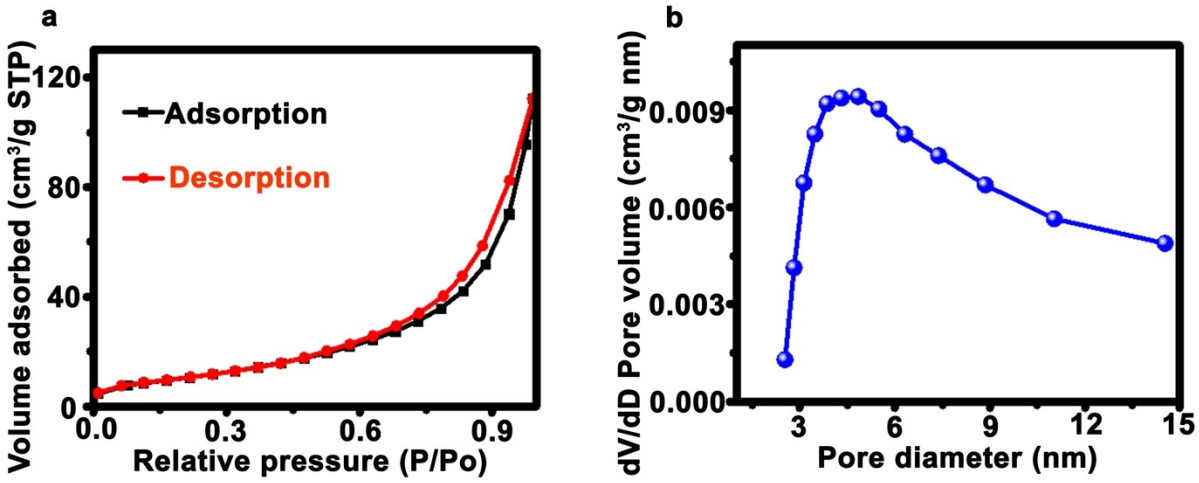

Fig. S24 BET characterization of the 88-h UV irradiated SiNNs. (a) Nitrogen adsorption-desorption isotherms and (b) BJH pore size distribution calculated from N_2 adsorption isothermals of the 88-h UV irradiated SiNNs.

As shown in Fig. S24a, nitrogen adsorption-desorption isotherms are measured to investigate the surface area and the pore size distribution of the 88-h UV irradiated SiNNs sample. The general shape of the N_2 sorption isotherms for the 88-h UV irradiated SiNNs suggests the existence of different pore sizes spanning from micro to macropores (Fig. S24a). Fig. S24b shows the pore size distributions of the 88-h UV irradiated SiNNs sample calculated from the nitrogen adsorption branch. The BET surface area and the Barrett-Joyner-Halenda (BJH) average pore size of SiNNs are 37 m^2/g, and 6.9 nm, respectively. In comparison to the 0-h UV irradiated SiNNs of 120 m^2/g in BET surface area (that is SiNNs, Fig. S4), the 88-h UV irradiated SiNNs exhibit distinctly smaller BET surface area (37 m^2/g) due to damage of the network structure of SiNNs induced by long-term intense UV irradiation.

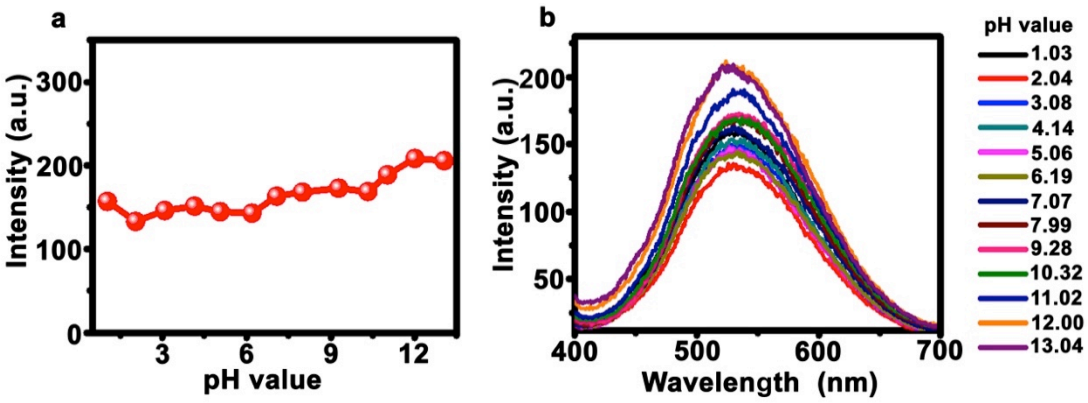

Fig. S25 (a) Temporal evolution of the SiNNs fluorescence in water under various pH values. (b) The corresponding PL spectra of the SiNNs in water under various pH values. As shown in Fig. S25, the resultant SiNNs maintain strong PL in the wide pH range of 1-13, which show fluctuation to some extent (less than ~20%) in acidic-to-basic environments. These experimental results suggest that the SiNNs feature robust pH-stability.

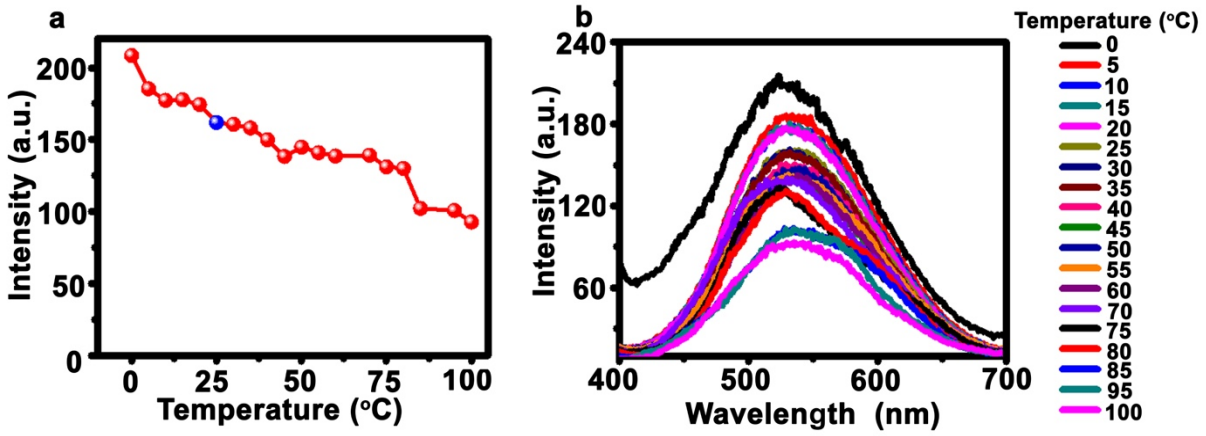

Fig. S26 (a) Temporal evolution of the fluorescence of the SiNNs under various temperatures. (b) The corresponding PL spectra of the SiNNs under different temperature. The blue point indicates that original PL intensity (~162) of the SiNNs under room temperature 25 ^{o}C. As shown in Fig. S26, the fluorescent signal of the SiNNs enhances with decreasing temperature. The fluorescent intensity of the SiNNs can up to ~208 at 0 ^{o}C, which increases by ~28%. In contrast, the PL intensity of the SiNNs gradually reduces with increasing temperature, which decreases by ~43% in the range of 25-100 ^{o}C. The temperature stability result indicates that the fluorescence of the SiNNs is unstable at high temperature, which will be quenched to some extent.

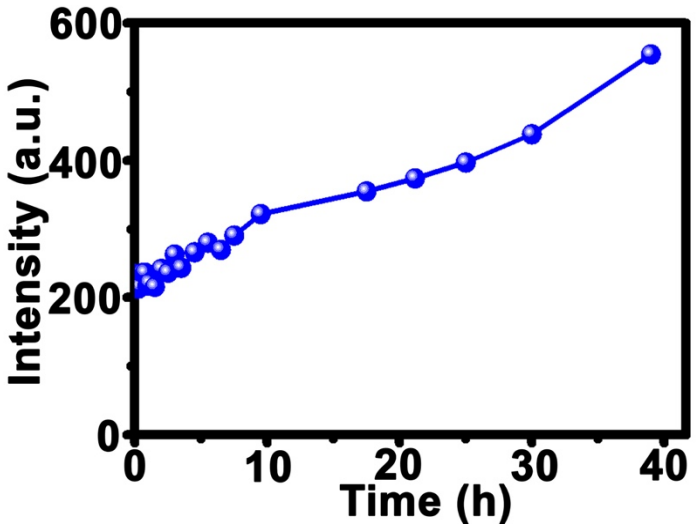

Fig. S27 Photostability of the SiNNs prepared under 120 ^{o}C/3h. The fluorescent intensity of the SiNNs increases gradually with the increase of UV irradiation time, circa 1.4 times increases of fluorescent intensity of the SiNNs is observed after 39 h UV irradiation. The SiNNs synthesized under 120 ^{o}C/ 3h exhibit similar photostability to the SiNNs synthesized under 120 ^{o}C/1h (e.g., Fig. 3a).

3. References

1 Y. L. Zhong, X. T. Sun, S. Y. Wang, F. Peng, F. Bao, Y. Y. Su, Y. Y. Li, S. T. Lee, Y. He, *ACS Nano*, 2015, **9**, 5958-5967.

2 Y. He, Y. L. Zhong, F. Peng, X. P. Wei, Y. Y. Su, Y. M. Lu, S. Su, W. Gu, L. S. Liao, S. T. Lee, *J. Am. Chem. Soc.*, 2011, **133**, 14192-14195.

3 Y. L. Zhong, F. Peng, F. Bao, S. Y. Wang, X. Y. Ji, L. Yang, Y. Y. Su, S. T. Lee, Y. He, *J. Am. Chem. Soc.*, 2013, **135**, 8350-8356.

4 S. C. Wu, Y. L. Zhong, Y. F. Zhou, B. Song, B. B. Chu, X. Y. Ji, Y. Y. Wu, Y. Y. Su, Y. He, *J. Am. Chem. Soc.*, 2015, **137**, 14726-14732.

5 L. Yang, Y. Liu, Y. L. Zhong, X. X. Jiang, B. Song, X. Y. Ji, Y. Y. Su, L. S. Liao, Y. He, *Appl. Phys. Lett.*, 2015, **106**, 173109.

6 Y. L. Zhong, F. Peng, X. P. Wei, Y. F. Zhou, J. Wang, X. X. Jiang, Y. Y. Su, S. Su, S. T. Lee, Y. He, *Angew. Chem. Int. Ed.*, 2012, **51**, 8485-8489.

7 J. Y. Pang, Y. Y. Su, Y. L. Zhong, F. Peng, B. Song and Y. He, *Nano Res.*, 2016, **9**, 3027-3037.

8 R. A. A. Muzzarelli, F. Tanfani, M. Emanuelli and S. Mariotti, *Carbohydr. Res.*, 1982, **107**, 199-214.

9 M. Thanou, M. T. Nihot, M. Jansen, J. C. Verhoef and H. E. Junginger, *J. Pharm. Sci.*, 2001, **90**, 38-46.

10 K. S. Walton, R. Q. Snurr, *J. Am. Chem. Soc.*, 2007, **129**, 8552-8556.

11 B. Liu, H. Shioyama, H. L. Jiang, X. B. Zhang, Q. Xu, *Carbon*, 2010, **48**, 456-463.

12 B. Liu, H. Shioyama, T. Akita, Q. Xu, *J. Am. Chem. Soc.*, 2008, **130**, 5390-5391.

13 E. Stöckel, X. F. Wu, A. Trewin, C. D. Wood, R. Clowes, N. L. Campbell, J. T. A. Jones, Y. Z. Khimyak, D. J. Adams, A. I. Cooper, *Chem. Commun.*, 2009, 212-214.

14 P. J. Beldon, L. Fábián, R. S. Stein, A. Thirumurugan, A. K. Cheetham, T. Friščić, *Angew. Chem. Int. Ed.*, 2010, **49**, 9640-9643.

15 K. S. Park, Z. Ni, A. P. Côté, J. Y. Choi, R. D. Huang, F. J. Uribe-Romo, H. K. Chae, M. O'Keefe, O. M. Yaghi, *Proc. Natl. Acad. Sci. USA*, 2006, **103**, 10186-10191.

16 M. Tu, S. Wannapaiboon, K. Khaletskaya, R. A. Fischer, *Adv. Funct. Mater.*, 2015, **25**, 4470-4479.

17 Y. Lo, C. H. Lam, C. W. Chang, A. C. Yang, D. Y. Kang, *RSC Adv.*, 2016, **6**, 89148-89156.

18 B. Liu, M. P. Jian, R. P. Liu, J. F. Yao, X. W. Zhang, *Colloids and Surfaces A: Physicochem. Eng. Aspects*, 2015, **481**, 358-366.

19 E. Vinogradova, M. Estrada, A. J. Moreno, *Colloid Interf. Sci.*, 2006, **298**, 209-212.

20 G. De, B. Karmakar, D. Ganguli, *J. Mater. Chem.*, 2000, **10**, 2289-2293.

21 B. Song, Y. L. Zhong, S. C. Wu, B. B. Chu, Y. Y. Su, Y. He, *J. Am. Chem. Soc.*, 2016, **138**, 4824-4831.

22 B. Song, H. Y. Wang, Y. L. Zhong, B. B. Chu, Y. Y. Su, Y. He, *Nanoscale*, 2018, **10**, 1617-1621.

23 Y. Y. Wu, Y. L. Zhong, B. B. Chu, B. Sun, B. Song, S. C. Wu, Y. Y. Su, Y. He, *Chem. Commun.*, 2016, **52**, 7047-7050.

24 R. K. Brow, *J. Non-Cryst. Solids*, 1996, **184**, 267.

25 M. N. Islam, T. B. Ghosh, K. L. Chopra, H. N. Acharya, *Thin Solid Films*, 1996, **280**, 20-25.

26 R. V. Siriwardane, J. A. Poston Jra, E. P. Fisher, M. S. Shen, A. L. Miltz, *Appl. Surf. Sci.*, 1999, **152**, 219-236.

27 S. Bera, A. A. M. Prince, S. Velmurugan, P. S. Raghavan, R. Gopalan, G. Panneerselvam, S. V. Narasimhan, *J. Mater. Sci.*, 2001, **36**, 5379-5384.

28 Y. He, Y. L. Zhong, F. Peng, X. P. Wei, Y. Y. Su, S. Su, W. Gu, L. S. Liao, S. T. Lee, *Angew. Chem. Int. Ed.*, 2011, **50**, 3080-3083.

29 C. Kirchner, T. Liedl, S. Kudera, T. Pellegrino, A. M. Javier, H. E. Gaub, S. Stölzle, N. Fertig, W. J. Parak, *Nano Lett.*, 2005, **5**, 331-338.

30 Y. He, H. T. Lu, L. M. Sai, Y. Y. Su, M. Hu, C. H. Fan, W. Huang, L. H. Wang, *Adv. Mater.*, 2008, **20**, 3416-3421.

31 Y. Y. Su, Y. He, H. T. Lu, L. M. Sai, Q. N. Li, W. X. Li, L. H. Wang, P. P. Shen, Q. Huang, C. H. Fan, *Biomaterials*, 2009, **30**, 19-25.

32 H. Q. Shi, W. N. Li, L. W. Sun, Y. Liu, H. M. Xiao, S. Y. Fu, *Chem. Commun.*, 2011, **47**, 11921-11923.